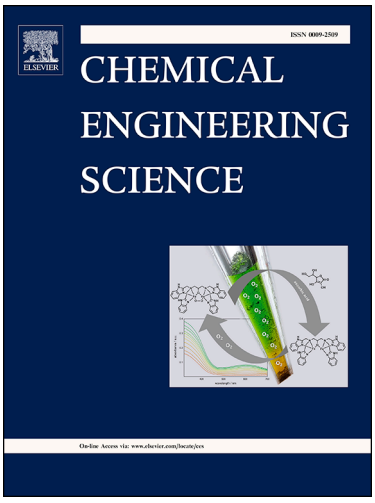

Coalescence of small bubbles with surfactants

Jiakai Lu, Carlos M. Corvalan, Y.M. John Chew, Jen-Yi Huang

PII: S0009-2509(18)30780-2
DOI: https://doi.org/10.1016/j.ces.2018.11.002
Reference: CES 14590

To appear in: *Chemical Engineering Science*

Received Date: 21 April 2018
Accepted Date: 2 November 2018

Please cite this article as: J. Lu, C.M. Corvalan, Y.M.J. Chew, J-Y. Huang, Coalescence of small bubbles with surfactants, *Chemical Engineering Science* (2018), doi: https://doi.org/10.1016/j.ces.2018.11.002

Coalescence of small bubbles with surfactants

Jiakai Lu[1], Carlos M. Corvalan[1], Y.M. John Chew[a], Jen-Yi Huang[1]

Department of Food Science, Purdue University, West Lafayette, IN 47907, USA

[a]*Department of Chemical Engineering, University of Bath, Building 9 West, Bath BA2 7AY, UK*

Abstract

Bubble coalescence is central to many important technological processes, such as separations, cleaning of oil spills, microfluidics, emulsification and foaming. It is well known that surfactants, which are frequently present as additives or contaminants, delay coalescence by slowing the drainage of the liquid film separating the approaching bubbles before they make contact. However, the coalescence and surfactant transport mechanisms developed after surfactant-laden bubbles make initial contact remain poorly understood. Here, we characterize these mechanisms using high-fidelity numerical simulations to predict the evolution of bubble interfaces, surfactant spreading, and induced Marangoni flows. Our results show that the surfactant initially accumulates on the tiny meniscus bridge formed between the coalescing bubbles due to the rapid and highly localized contraction of meniscus area. At the same time, a Marangoni-driven convective flow is generated at the interface, which drags the accumulated surfactant away from the joining meniscus and toward the back of the bubbles. Together, these transport mechanisms af-

*Jen-Yi Huang

Email address: huang874@purdue.edu (Jen-Yi Huang)

fect the rate bubble coalescence by dynamically modifying the local pull of surface tension on the bubble interfaces.

Keywords: Microbubble, Surfactant, Interface, Simulation, Transport phenomena, Coalescence

1. Introduction

Gas-in-liquid mixtures, i.e., bubbles dispersed in a continuous liquid medium, are ubiquitous in everyday life and many industrial processes. Typical examples of unit operations that utilize gas-in-liquid mixtures include bubble columns, aggregative fluidized beds, spray driers, sparged aerators, stirred bioreactors, all of which are used extensively in food, polymer, biochemical, and other processing applications (Chhabra and Richardson, 1999). The flow of bubbles is useful to facilitate momentum, heat and mass transport by enhancing mixing and turbulence (Kandlikar, 2013). Bubbles are also used in cleaning processes of medical devices such as in ultrasonication (Mason, 1997). However, the presence of bubbles is sometimes undesirable as they affect the quality of final products, such as in photographic, paper and glass industries (Samanta and Ghosh, 2011).

The single most important feature of bubbles that sets them apart from rigid solid particles is their mobile interface and their ability to deform and resist to shearing forces while remaining in static equilibrium. The flow behavior of bubbles is largely influenced by the type and relative magnitude of forces present in the continuous phase. Therefore, the bubbles exhibit a wide variety of shapes such as spherical cap, slug or bubbly, which may change with time and position during the course of its movement in a piece

of equipment (Clift, 1978). Thermal and physical properties of the gas and liquid also affect the bubble dynamics. In a gas-in-liquid process application, bubbles constantly collide with each other. Depending upon the bubble size, their velocity, interfacial chemistry and the frequency of collisions, bubbles may break or coalesce. Coalescence may be desirable (such as in promoting separation by foaming) or detrimental (such as in chemical reactors where it is desirable to have large interfacial area) to a process depending upon the application. A solid understanding of the principle of bubble dynamics is thus critically important to the rational design and operation of industrial processes.

Current interests in bubble dynamics include understanding the interaction between the characteristics of fluid (i.e., Newtonian and non-Newtonian) and the physics and kinematics of flow. Reliable and accurate calculations for process design frequently require key quantitative information on the free rise velocity, heat and mass transfer, breakage and coalescence behaviors. For instance, aeration is an essential component of wastewater treatment and is usually achieved by bubbling air through water. However, the current processes are highly inefficient and account for a considerable amount of operational cost of these plants because their design and operating conditions are far from optimum. The inefficient mass transfer is generally caused by relatively small gas-liquid interfacial area of large bubbles termed macrobubbles (several millimeters in diameter) and the short bubble-in-water retention time (i.e., high rising velocity). Microbubbles, i.e., small scale bubbles with diameter in the range between 10 and 200 microns, have large surface-to-volume ratio and hence provide a significantly larger gas-liquid interfacial

area than macrobubbles (Khuntia et al., 2012). The microbubbles also have higher stability and longer retention time in water.

It is well established that the phenomenon of coalescence entails three stages: initial approach of the bubbles, controlled essentially by the hydrodynamics of the bulk liquid, which results in a film with the thickness of a few microns separating the two bubbles. The second step is the gradual thinning of this film to a few Angstroms. The rate of film thinning and drainage in the second step determines whether bubble contact and coalescence will occur or not. If the time required to drain the film to reach the rupturing thickness level is longer than the period of contact, the two bubbles may separate rather than coalesce. The rate of film thinning and drainage is determined by the hydrodynamics of thin films. The final third stage is the rupturing of the film leading to the actual contact and coalescence of the two bubbles. Coalescence of air bubbles is greatly influenced by the interfacial chemistry. In most industrial applications, additives or surfactants are often used to control the bulk or interfacial properties of solutions (Lessard and Zieminski, 1971). Although the behavior of approaching bubbles is known to be strongly affected by the presence of surfactants, the detailed interfacial transport mechanisms by which surfactants affects the coalescence dynamics after the bubbles are brought into contact is still an open question. Indeed, most studies on surfactant-laden bubbles have focused on the influence of surfactants delaying the drainage of the thin liquid film separating the approaching bubbles (Chan et al., 2011), but how surfactants influence coalescence after the bubbles make initial contact is still unclear.

Here we characterize the mechanism of coalescence of surfactant-laden

bubbles after the bubbles make contact using direct numerical simulation (DNS) (Scardovelli and Zaleski, 1999). Contrary to interface capturing methods that typically utilize an indicator function to implicitly describe the phase interface (James and Lowengrub, 2004; Alke and Bothe, 2009; Ceniceros, 2003), the direct numerical simulations solve the full Navier-Stokes system that governs the free-surface hydrodynamics coupled to the convection-diffusion equation that governs the surfactant transport using an arbitrary-Lagrangian-Eulerian (ALE) scheme to explicitly track the deforming bubble interface. Compared with other interface tracking method such as boundary integral method and front tracking method, the ALE based DNS method used in this study has the advantage of tracking large topological changes such as breakup and coalescence (Liu et al., 2018). We have previously successfully applied this method to other free-surface flows, including the breakup of thin liquid films (Lu et al., 2015), jets (Lu and Corvalan, 2014), and filaments (Muddu et al., 2012), as well as the study of the influence of surfactants in drop coalescence (Lu and Corvalan, 2012) and the collapse of micropores (Lu et al., 2018).

Results show – to our knowledge for the first time – that when the two bubbles covered with surfactant coalesce, surfactant initially accumulates on the tiny meniscus bridge formed between the bubbles as a consequence of the rapid contraction of the meniscus interfacial area. Marangoni flows induced by the resulting surface-tension gradients critically affect the subsequent surfactant distribution by dragging surfactant away from the meniscus bridge and towards the back of the bubbles. These coupled transport mechanisms affect the rate at which the bubbles coalesce by modulating the local pull of

surface tension on the bubble interfaces.

When two slowly approaching bubbles make contact, a tiny joining bridge forms between the bubbles, which then expands rapidly as the two bubbles merge into one. Here, we study the evolution of the bubble interfaces, surfactant spreading, and induced Marangoni flows developed during the merging of two identical gas micro-bubbles immersed in a quiescent external Newtonian liquid of constant density ρ and viscosity μ. Initially, the gas-liquid interface is covered with an insoluble surfactant of uniform concentration γ_0, as sketched in Figure 1.

We describe the system in dimensionless form using the bubble radius a as length scale, the viscous-capillary time $\tau \equiv a\mu/\sigma_0$ as timescale, and characteristic capillary pressure σ_0/a as stress scale, where σ_0 is the initial interfacial tension. As the coalescence process evolves, the changing local concentration of surfactant is measured in units of γ_0, and the corresponding dynamic surface tension is measured in units of σ_0.

The gas phase is considered dynamically inert, and the evolution of the velocity field $\mathbf{v}$ and pressure p in the surrounding liquid phase are characterized by solving the full axisymmetric Navier-Stokes and continuity equations:

$$\nabla \cdot \mathbf{v} = 0, \tag{1}$$

$$\frac{\partial \mathbf{v}}{\partial t} + \mathbf{v} \cdot \nabla \mathbf{v} = Oh^2 \ \nabla \cdot \mathbf{T}, \tag{2}$$

where the effect of gravity is considered negligible due to the small scale of the micro-bubbles. The Navier-Stokes system is solved consistent with the traction boundary condition at the gas-liquid interface:

$$2H\sigma\mathbf{n} + \nabla_s \sigma = \mathbf{n} \cdot \mathbf{T}, \tag{3}$$

where $\mathbf{T} = -p\mathbf{I} + (\nabla\mathbf{v} + \nabla\mathbf{v}^T)$ is the Cauchy stress tensor, H the interfacial curvature, $\mathbf{n}$ the unit normal vector, and $\nabla_s\sigma \equiv (\mathbf{I} - \mathbf{nn}) \cdot \nabla\sigma$ the interfacial gradient of surface tension (Slattery, 1990). There is no mass transfer across the phase interface, which is ensured by the kinematic interfacial condition

$$\mathbf{n} \cdot (\mathbf{v} - \mathbf{v}_s) = 0, \tag{4}$$

where $\mathbf{v}_s$ is the velocity of the liquid at the air-liquid interface. To focus on the effect of surfactant on the coalescence dynamics, we set the Ohnesorge number $Oh \equiv \mu/\sqrt{\rho a \sigma_0}$ to that of a liquid with moderate viscosity, $Oh = 0.1$, except where specifically stated. The bubbles are axisymmetric about the centerline $r = 0$ and symmetric about the midplane $z = 0$.

The first term in equation (3) represents the normal capillary stress and the second term represents the tangential Marangoni stress. Both, through surface tension, depend on the distribution of surfactant concentration γ on the interface, which is governed by the transport equation (Wong et al., 1996)

$$(\partial\gamma/\partial t)_s + \gamma(\mathbf{v}_s \cdot \mathbf{n})(\nabla_s \cdot \mathbf{n}) + \nabla_s \cdot (\gamma\mathbf{v}_s \cdot \mathbf{t})\mathbf{t} - Pe^{-1}\nabla_s^2\gamma = 0, \tag{5}$$

where $\mathbf{t}$ is the unit vector tangent to the interface. The transport equation includes changes in concentration due to convection, diffusion and contraction of the surface area. The surfactant diffusion coefficient D is typically small, and thus the Peclet number, defined as the ration between the diffusion time scale a^2/D and viscous capillary time scale τ, $Pe \equiv (a^2/D)/\tau$ is set to 1×10^3 in our simulations. Following Hansen et al. (1999), Campana et al. (2004) and Dravid et al. (2006), we consider that for dilute surfactants the equation of state is approximately linear $\sigma = 1 - \beta(\gamma - 1)$, and thus the

surfactant strength is characterized by the Elasticity (or Marangoni) number β (Campana et al., 2004).

The numerical method used to solve the governing equations is identical to the method we have successfully applied to other free-surface flows with surfactant and thus is only briefly summarized here; for a detailed description of the algorithm the reader is referred to (Xue et al., 2008; Muddu et al., 2012; Lu et al., 2018). The governing equations (1), (2), (4) and (5) that couple the free surface hydrodynamics and interfacial mass transport are simultaneously solved using a Galerkin/finite element method for spatial discretization, along with an arbitrary Lagrangian-Eulerian (ALE) method of spines to accurately trace the gas-liquid interface (Xue et al., 2008; Muddu et al., 2012; Lu et al., 2018). The time derivatives are discretized using an implicit finite difference predictor-corrector with adaptive time-step (Corvalan and Saita, 1991), and the surfactant transport is incorporated into the system following the method described in detail in Campana et al. (2004). Finally, the set of coupled non-linear equations resulting from the spatial and temporal discretization is simultaneously solved by Newton's method using an analytical Jacobian matrix to enhance the radius of convergence (Kistler and Scriven, 1983). Studies were carried out with different grid densities, and grids ranging between approximately 7000-8000 degrees of freedom were selected for the simulations. The elements were non-uniformly spaced with higher concentration of elements in the vicinity of the meniscus connecting the bubbles in the axial direction and near the moving interface in the radial direction.

2. Results and Discussion

Coalescence Dynamics

To gain an initial insight into the effects of surfactant on the coalescence dynamics, we first present in Figure 2a the evolution of the interfacial shapes of small bubbles without the presence of surfactant. At the time of initial contact the bubbles are connected by a tiny neck, which then grows driven by the pull of surface tension forces on the highly curved meniscus around the neck. Here, the relative importance of viscous to inertia and surface tension forces is characterized by the Ohnesorge number $Oh = 10^{-1} \ll 1$, and thus the process is essentially governed by capillarity and inertia.

By solving the full Navier-Stokes equations, the direct numerical simulations enable accurate characterization of the coalescing dynamics from the early stages of initial contact to the later stages of merging into one bigger bubble. Indeed, early-time results in the enlarged view in Figure 2b demonstrate that the predicted neck radius r_m (solid line) compares well with the measurements from recent high-speed visualization experiments by Paulsen et al. (2014) (symbols). Similarly, later-time ($t > 60$) predictions in Figure 2c show an excellent agreement with the theoretical radius corresponding to the eventual equilibrium bubble. Specifically, results show that the computed neck radii oscillate around the theoretical value $r_b = 2^{1/3}$ (dashed line) as the bubbles alternate between oblate and prolate shapes, converging toward this expected value as $t \to \infty$.

Results in Figure 2c compare the evolution of predicted bubble neck radius for bubbles with clean interface (black line) and with a moderate surfactant of Elasticity number $\beta = 1$ (blue line). Because our focus is on the

effects of the surfactant migration and the resulting gradients of interfacial tension (Marangoni stresses), both systems start with identical dimensionless surface tension $\sigma = 1$ (or $\hat{\sigma} = \sigma_0$ in dimensional terms). The figure makes clear that both systems initially coalesce at essentially the same speed. However, after the neck radius grows to $r_b \approx 1$, changes in interfacial tension and Marangoni stresses resulting from the redistribution of surfactant on the interface significantly reduce the speed of coalescence of the surfactant-laden bubbles. As a result, it took about $t = 60$ for the bubbles with $\beta = 1$ and about $t = 45$ for the bubbles with clean interface to coalesce, indicating a significant difference in the time of coalescence despite the fact that both systems begin with identical surface tension. Here we have defined the time of coalescence, somewhat arbitrarily, as the shortest time after which r_b differs by less than 1% from the radius of the final spherical bubble.

Surfactant Transport

Having exemplified how the redistribution of surfactant influences the overall coalescence dynamics, we now seek to understand in more detail the transport mechanisms responsible for this redistribution; that is, how the initially evenly distributed surfactant accumulates and migrates dynamically on the bubble interface. By solving the interfacial surfactant transport fully coupled to the free-surface flow, the simulations enable for the first time a detailed mapping of the surfactant migration patterns on the bubble interface. These patterns, summarized in Figure 3, demonstrate that the surface active species briefly accumulate on the joining meniscus bridge at the incipience of coalescence (red line) and then migrate, assisted by Marangoni stresses, first away from the meniscus (blue line) and then all the way to the back of

the bubbles (black line).

The initial accumulation of surfactant occurs because of the rapid contraction of of the interface during the initial opening of the neck. As the bubbles coalesce, the interfacial area contracts at widely different rates, both spatial and temporal. The rate of area contraction $(\mathbf{v}_s \cdot \mathbf{n})(\nabla_s \cdot \mathbf{n})$ depends on the local interfacial speed $(\mathbf{v}_s \cdot \mathbf{n})$ and curvature $(\nabla_s \cdot \mathbf{n})$ (see Equation 5), and thus is most important at the incipience of coalescence due to the rapid motion of the highly curved meniscus. The overall process is illustrated in Figure 4, which shows that, as the interface contracts due to the advancing meniscus (Figure 4a), the local surfactant concentration grows rapidly (Figure 4b). The accumulation process occurs in a comparatively short period, which in this example span about 0.1 capillary times.

After reaching a maximum, the surfactant concentration decreases steadily as the accumulated surfactant is dragged away from the meniscus by the adjacent capillary flow. Indeed, as the neck radius grows the rate of area contraction slows down and the fluid near the meniscus accelerates driven by the capillary pressure. Eventually, the meniscus cannot contract fast enough to balance the convective flow, and the dominant mode of surfactant transport changes from surfactant crowding on the meniscus area to surfactant migration along the interface. Figure 5 demonstrates this transport mechanism, showing the spatial and temporal evolution of the surfactant as the concentration peak migrates symmetrically (red line), first away from the meniscus (black line), and then up the sides of the bubbles (blue line).

Effect of Marangoni Stresses

Our results show that the Marangoni stresses play a critical role in the fast transport of the accumulated surfactant away from the meniscus. The initial contraction of the meniscus area not only increases the local surfactant concentration but also leads to steep surface tension gradients. Consequently, tangential Marangoni stresses $\mathbf{n} \cdot \mathbf{T} \cdot \mathbf{t} = \nabla_s \sigma$ develop in the vicinity of the meniscus pulling the fluid adjacent to the interface towards the regions of high surface tension (Equation 3).

After the initial opening, the coalescence dynamics progresses as illustrated in Figure 6. The figure makes it clear that by the time the neck radius has grown to $r_m \approx 1$ the surfactant peak has reached the crest of the bubbles (Figure 6e), and then continues to migrate toward the back of the bubbles driven by the convective flow and the (Marangoni) interfacial stresses (Figure 6f). Eventually, the back of the bubbles are covered with excess surfactant (see also Figure 3), and the weakened local interfacial tension delays the axial merging motion.

The important role of the Marangoni stresses is illustrated in Figure 7, which shows radial velocity contours in the vicinity of the meniscus for different values of the elasticity number. Although the plots correspond to the same neck radius, the upward convective flow adjacent to the interface (here red is upwards and blue is downward) is noticeably more advanced for the bubbles of larger elasticity numbers due to the stronger Marangoni stresses.

Cross sectional radial velocity profiles shown in Figure 8 further demonstrate the strong influence of Marangoni stresses in the flow field. For the bubbles without surfactant (Figure 8a) the cross sectional velocity is maxi-

mum at the center ($z = 0$) and minimum at the interface (blue line), which is indicative of a (capillary) pressure driven flow. However, the velocity profile switches dramatically for the bubbles of larger elasticity number (Figures 8b). As the Marangoni stresses drag the liquid adjacent to the interface up the side of the bubbles through momentum transfer, the radial velocity becomes maximum at the interface and minimum at the center. Clearly, the non-linear dynamics initiated by the accumulated surfactant develops Marangoni flows that contribute strongly to its own dispersal.

3. Conclusion

We have performed direct numerical simulations to investigate the mechanisms of coalescence of surfactant-laden micro-bubbles after they make contact. Results show that surfactant initially accumulates on the tiny meniscus bridge formed between the bubbles due to the uneven and rapid contraction of meniscus interfacial area. As a result of the large surface-tension gradient, Marangoni flows critically affect the subsequent surfactant distribution by dragging surfactant away from the meniscus bridge and towards the back of the bubbles. Therefore, the rate of bubble coalescence is retarded by these coupled transport mechanisms on the interfaces.

These findings provide new mechanistic insights into the flow physics of surfactant-laden micro-bubble coalescence that enable optimization of process design. In addition, these new findings suggest new directions for future studies. For example, considering the influence of the imbalance of surfactant during the coalescence of micro-bubbles. In addition, although our direct numerical simulations solve the full Navier—Stokes system that gov-

erns the free-surface flow along with the full convection—diffusion equation that governs the interfacial surfactant transport, the results are still limited by simplified constitutive assumptions, including negligible surfactant solubility and linear surface equation of state. We expect that our results would motivate the further development of simulations that incorporate soluble surfactants. We also expect that our results would motivate detailed comparison between the dynamics of surfactant transport during bubble coalescence and drop coalescence. These two dynamics may differ substantially because Marangoni stresses act on different sides of the interface during bubble and drop coalescence as suggested by our previous work on surfactant laden drops (Lu and Corvalan, 2012).

Acknowledgments

This project was partially supported by the USDA National Institute of Food and Agriculture, AFRI project 2017-05024 and Hatch projects 1014964, 1008409 and 199888, and Purdue Research Foundation (PRF).

References

Alke, A., Bothe, D., 2009. 3d numerical modeling of soluble surfactant at fluidic interfaces based on the volume-of-fluid method. FDMP 1, 1–29.

Campana, D., Paolo, J. D., Saita, F. A., 2004. A 2-d model of rayleigh instability in capillary tubes – surfactant effects. International Journal of Multiphase Flow 50 (5), 431–454.

Ceniceros, H. D., 2003. The effects of surfactants on the formation and evolution of capillary waves. Physics of Fluids 15 (1), 245–256.

Chan, D. Y., Klaseboer, E., Manica, R., 2011. Film drainage and coalescence between deformable drops and bubbles. Soft Matter 7 (6), 2235–2264.

Chhabra, R. P., Richardson, J. F., 1999. Non-Newtonian Flow: Fundamentals and Engineering Applications. Butterworth-Heinemann.

Clift, R., 1978. Bubbles. Drops and Particles.

Corvalan, C. M., Saita, F. A., 1991. Automatic stepsize control in continuation procedures. Computers & Chemical Engineering 15 (10), 729–739.

Dravid, V., Songsermpong, S., Xue, Z., Corvalan, C. M., Sojka, P. E., 2006. Two-dimensional modeling of the effects of insoluble surfactant on the breakup of a liquid filament. Chemical engineering science 61 (11), 3577–3585.

Hansen, S., Peters, G., Meijer, H., 1999. The effect of surfactant on the stability of a fluid filament embedded in a viscous fluid. Journal of Fluid Mechanics 382, 331–349.

James, A. J., Lowengrub, J., 2004. A surfactant-conserving volume-of-fluid method for interfacial flows with insoluble surfactant. Journal of computational physics 201 (2), 685–722.

Kandlikar, S., 2013. Controlling bubble motion over heated surface through evaporation momentum force to enhance pool boiling heat transfer. Applied Physics Letters 102 (5), 051611.

Khuntia, S., Majumder, S. K., Ghosh, P., 2012. Microbubble-aided water and wastewater purification: a review.

Kistler, S. F., Scriven, L. E., 1983. Coating Flow: Computational Analysis of Polymer Processing. Applied Science Publishers, New York.

Lessard, R. R., Zieminski, S. A., 1971. Bubble coalescence and gas transfer in aqueous electrolytic solutions. Industrial & Engineering Chemistry Fundamentals 10 (2), 260–269.

Liu, H., Ba, Y., Wu, L., Li, Z., Xi, G., Zhang, Y., 2018. A hybrid lattice boltzmann and finite difference method for droplet dynamics with insoluble surfactants. Journal of Fluid Mechanics 837, 381–412.

Lu, J., Campana, D. M. M., Corvalan, C. M., 2018. Contraction of surfactant-laden pores. Langmuir.

Lu, J., Corvalan, C. M., 2012. Coalescence of viscous drops with surfactants. Chemical Engineering Science 78, 9–13.

Lu, J., Corvalan, C. M., 2014. Influence of viscosity on the impingement of laminar liquid jets. Chemical Engineering Science 119, 182 – 186.

Lu, J., Yu, J., Corvalan, C. M., 2015. Universal scaling law for the collapse of viscous nanopores. Langmuir 31 (31), 8618–8622.

Mason, T. J., 1997. Ultrasound in synthetic organic chemistry. Chemical Society Reviews 26 (6), 443–451.

Muddu, R. J., Lu, J., Sojka, P. E., Corvalan, C. M., 2012. Threshold wavelength on filaments of complex fluids. Chemical Engineering Science 69, 602–606.

Paulsen, J. D., Carmigniani, R., Kannan, A., Burton, J. C., Nagel, S. R., 2014. Coalescence of bubbles and drops in an outer fluid. Nature communications 5, 3182.

Samanta, S., Ghosh, P., 2011. Coalescence of air bubbles in aqueous solutions of alcohols and nonionic surfactants. Chemical engineering science 66 (20), 4824–4837.

Scardovelli, R., Zaleski, S., 1999. Direct numerical simulation of free-surface and interfacial flow. Annual Review of Fluid Mechanics 31, 567–603.

Slattery, J. C., 1990. Interfacial Transport Phenomena. Springer, New York.

Wong, H., Rumschitzki, D., Maldarelli, C., 1996. On the surfactant mass balance at a deforming fluid interface. Physics of Fluids (1994-present) 8 (11), 3203–3204.

Xue, Z., Corvalan, C. M., Dravid, V., Sojka, P. E., 2008. Breakup of shear-thinning liquid jets with surfactants. Chemical Engineering Science 63 (7), 1842–1849.

Figures

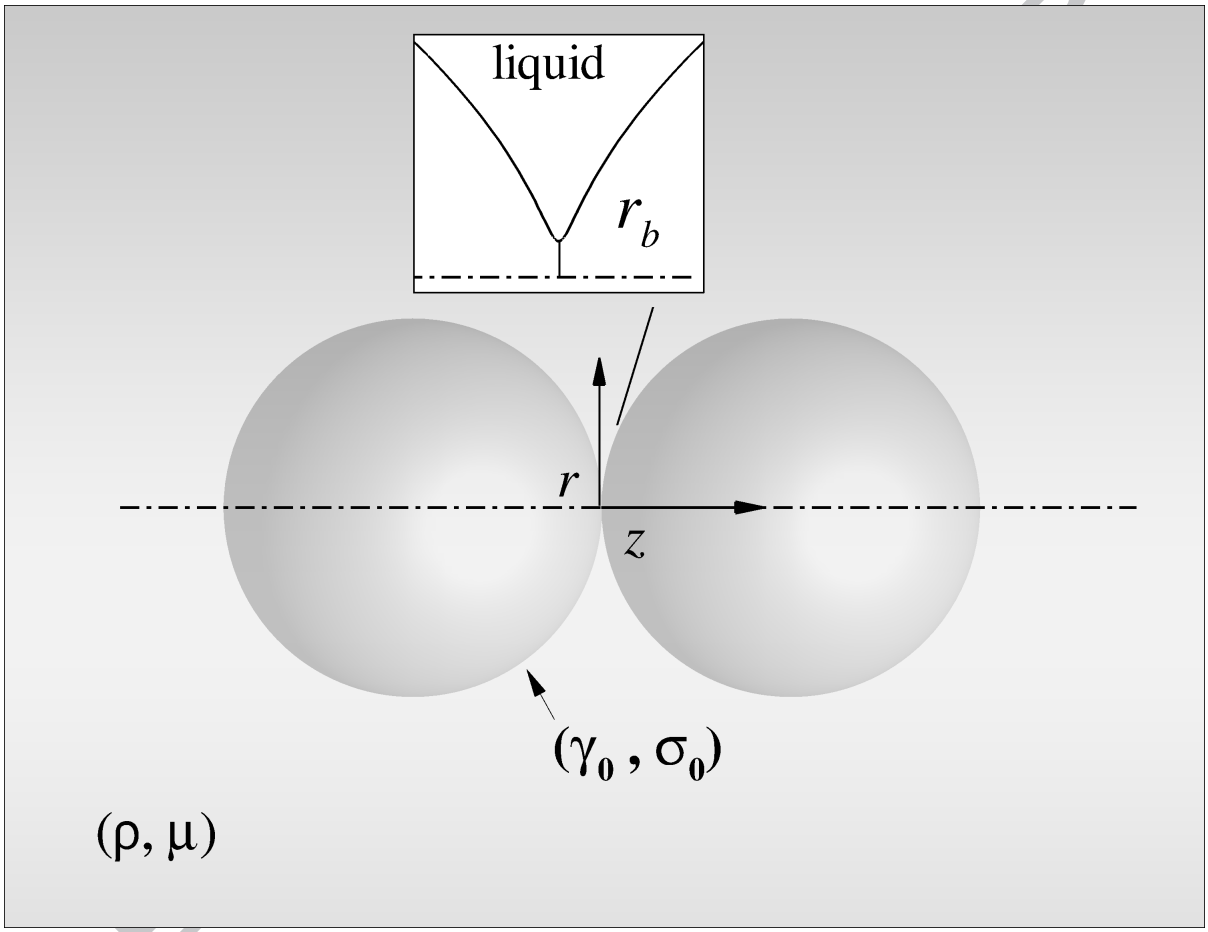

Figure 1: **Schematic of coalescing bubbles.** Two coalescing bubbles are connected by a small bridge (or neck) r_b (inset). The bubbles are immersed in an outer liquid of constant density ρ and viscosity μ. The initial surface tension σ_0 corresponds to a spatially uniform surfactant concentration γ_0. The bubble profile corresponds the case discussed in Fig.3b at time $t = 0.027$.

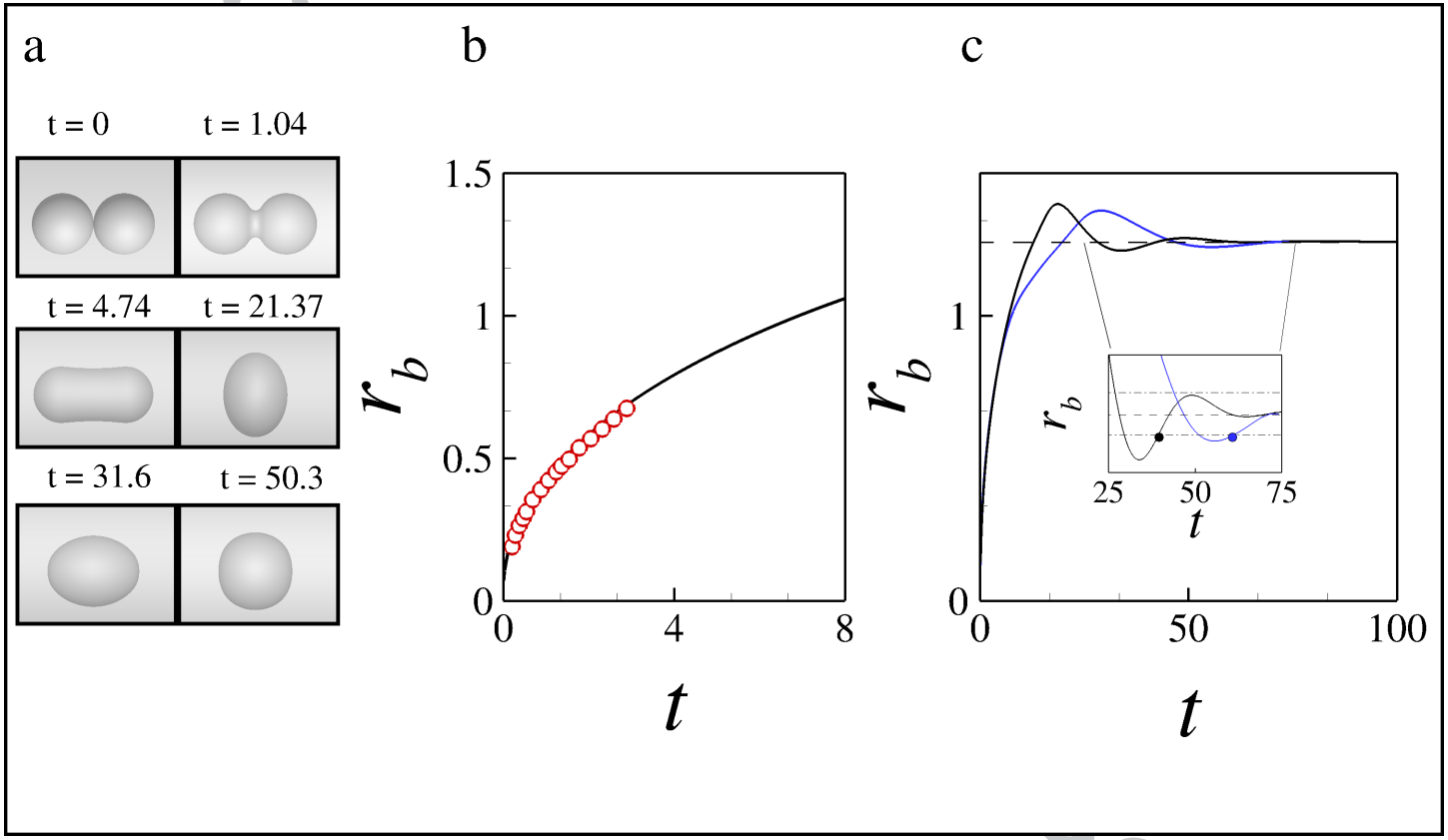

Figure 2: **Dynamics of bubble coalescence.** (a) Time evolution of the interfacial profiles for the coalescence of a pair of small bubbles in a fluid with $Oh = 0.1$ at times $t = 0, 1.04, 4.74, 21.37, 31.6$ and 50.3 Time evolution of radius of the bridge r_b connecting the bubbles with clean interface at both early times (b) and later times (c) and two bubbles with surfactant (blue). The predicted neck growth at early times show good agreement with experimental measurements by Paulsen et al. (2014) for a pair of pinned bubble coalescing in silicon oil with the $Oh \approx 1$ (red symbol). The dash dot lines in the inset in (c) marks 1% limit of the final radius and solids dots marks the coalescence time. Here $r_b(0) = 0.07$, and $\beta = 1$ for the bubbles with surfactant.

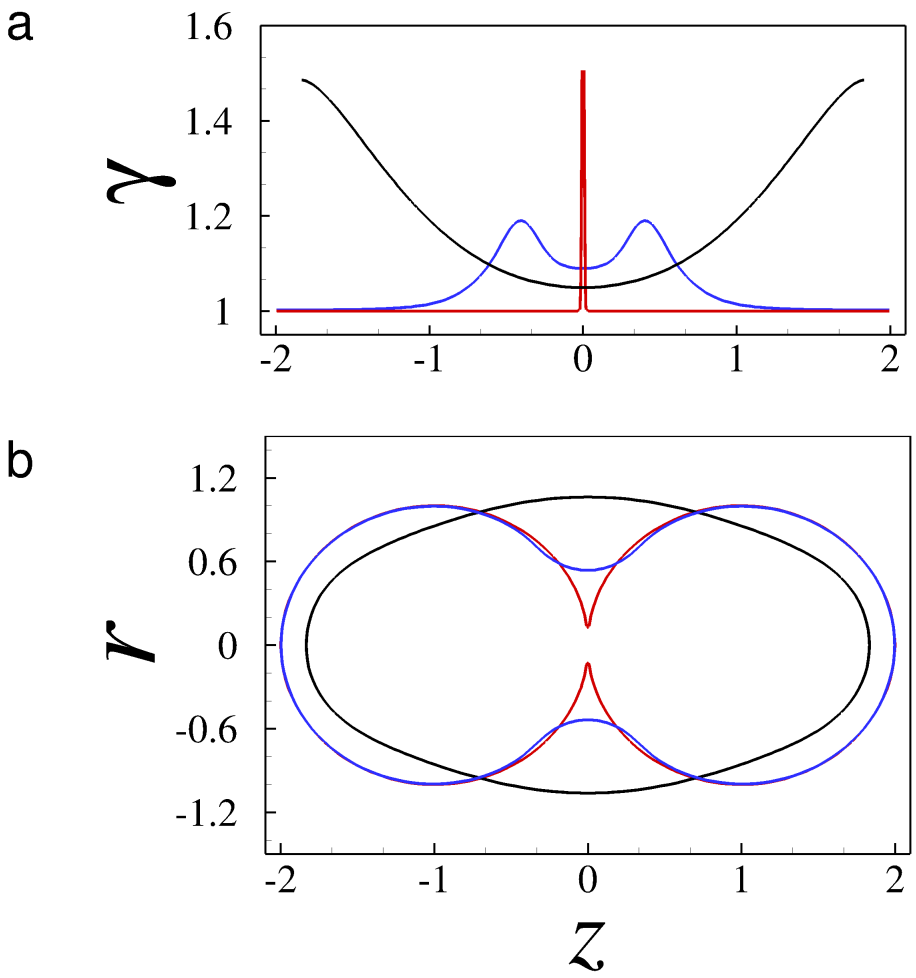

Figure 3: **Transport of surfactant at different stages of bubble coalescence.** (a) Distribution of surfactant concentration on the interface at early time $t = 0.027$ (red), intermediate time $t = 1.59$ (blue), and later time $t = 9.47$ (black) and (b) the corresponding interfacial profiles.Here $Oh = 0.1$, $r_b(0) = 0.07$, and $\beta = 1$.

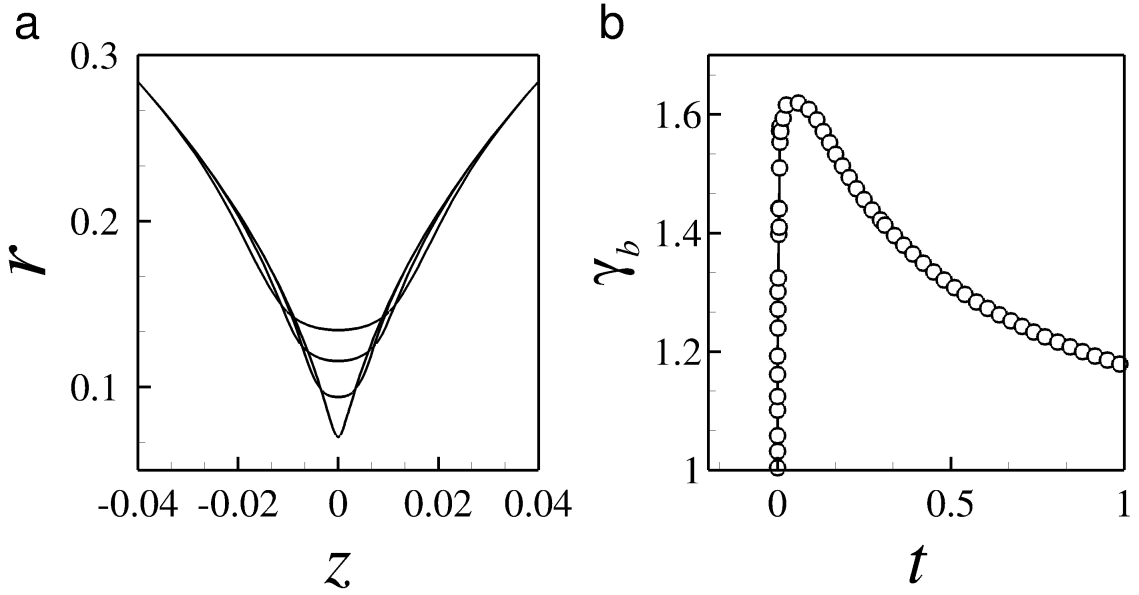

Figure 4: **Evolution of meniscus bridge profiles and surfactant concentration on the meniscus.** (a) Profiles of meniscus bridge connecting the two bubbles at early times $t = 0.0001, 0.018, 0.04$, and 0.058 show a rapid contraction of the local area, which increases local surfactant concentration on the meniscus when $t < 0.058$ (b). The surfactant concentration on the meniscus then decreases assisted by the convective capillary flow around the meniscus. Here $Oh = 0.1$, $r_b(0) = 0.07$, and $\beta = 1$.

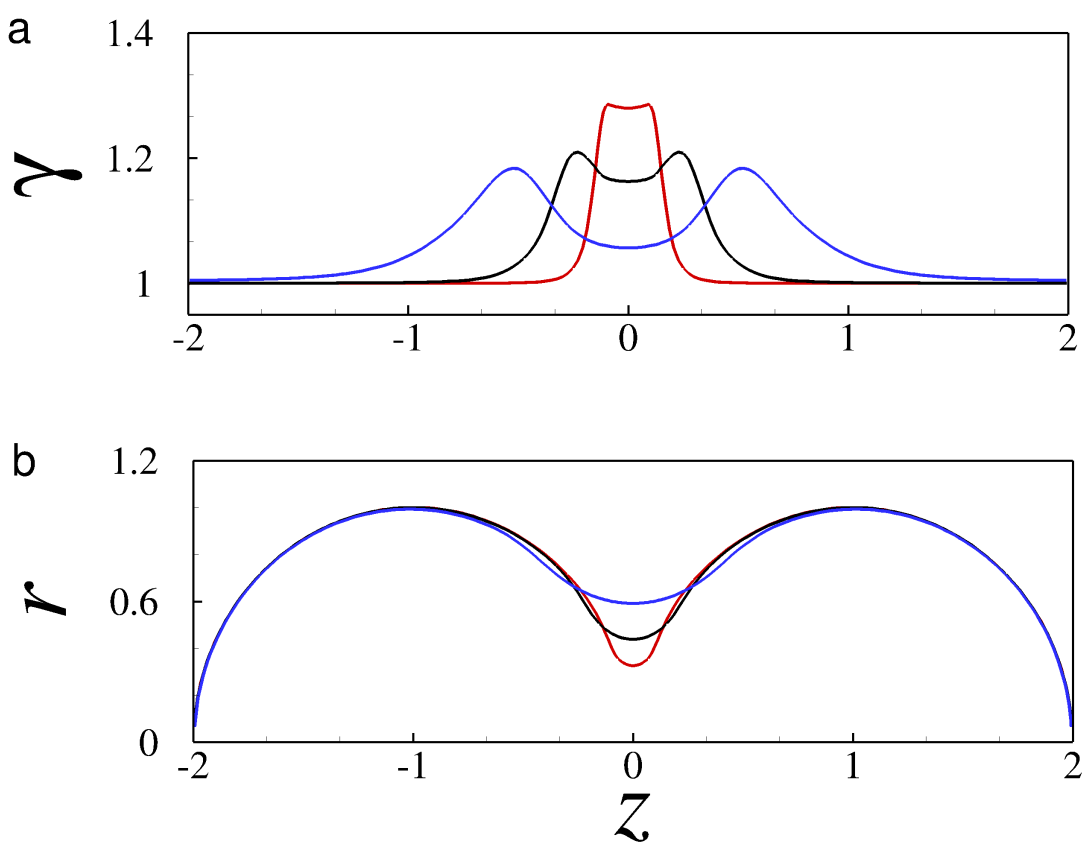

Figure 5: **Transport of surfactant away from the meniscus.** Surfactant concentration profiles (a) and corresponding interfacial shapes (b) at time $t = 0.5$ (red), $t = 1$ (black), and $t = 2$ (blue) show that the peak of surfactant spreads out symmetrically away from the neck. Here $Oh = 0.1$, $r_b(0) = 0.07$, and $\beta = 1$.

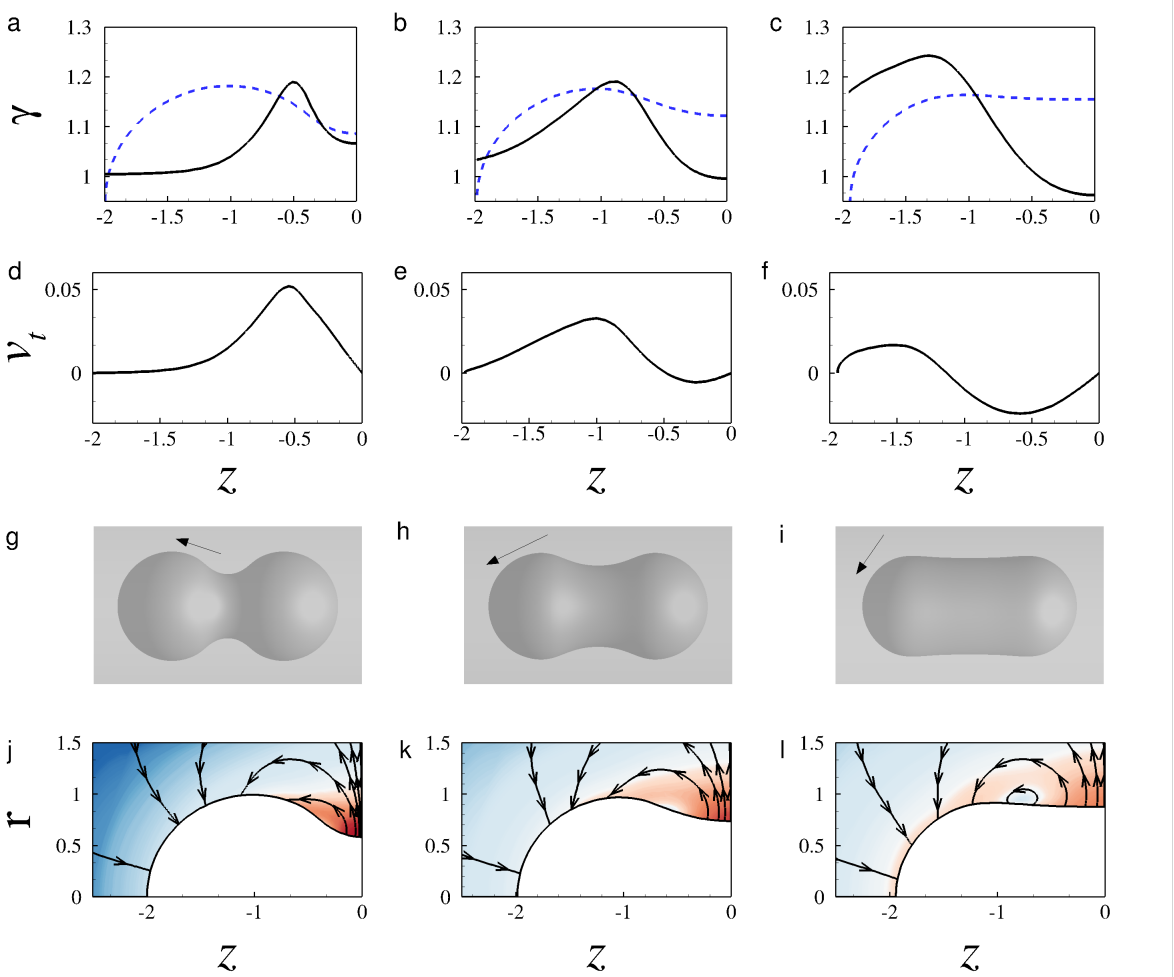

Figure 6: **Transport of surfactant towards the back of bubbles.** Surfactant concentration profiles (solid line) and corresponding interfacial shapes (dashed lines) for a quarter bubble at time $t = 1.97$(a), $t = 3.37$ (b), and $t = 4.88$ (c). The convective interfacial velocity (d)-(f) along with Marangoni stresses developed by the surface tension gradient drag the surfactant towards the back of the bubbles, indicated by the arrows in (g)-(i). (j)-(l) Instantaneous streamlines and velocity magnitude contours with red indicating large and blue indicating small in the fluid phase corresponding to the times in (a)-(c).

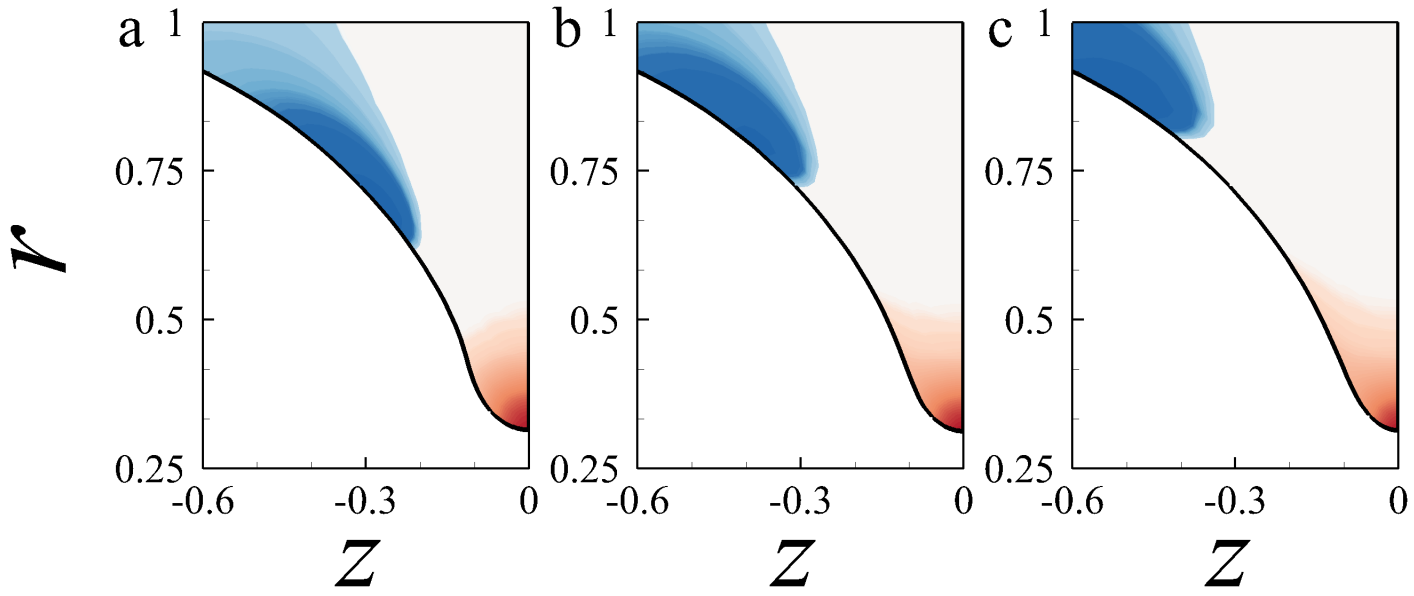

Figure 7: **Radial flow field.** Cross sectional radial velocity field with red indicating positive radial motion and blue indicating negative radial motion. Computations were carried out with elasticity numbers $\beta = 0$,1 and 5.

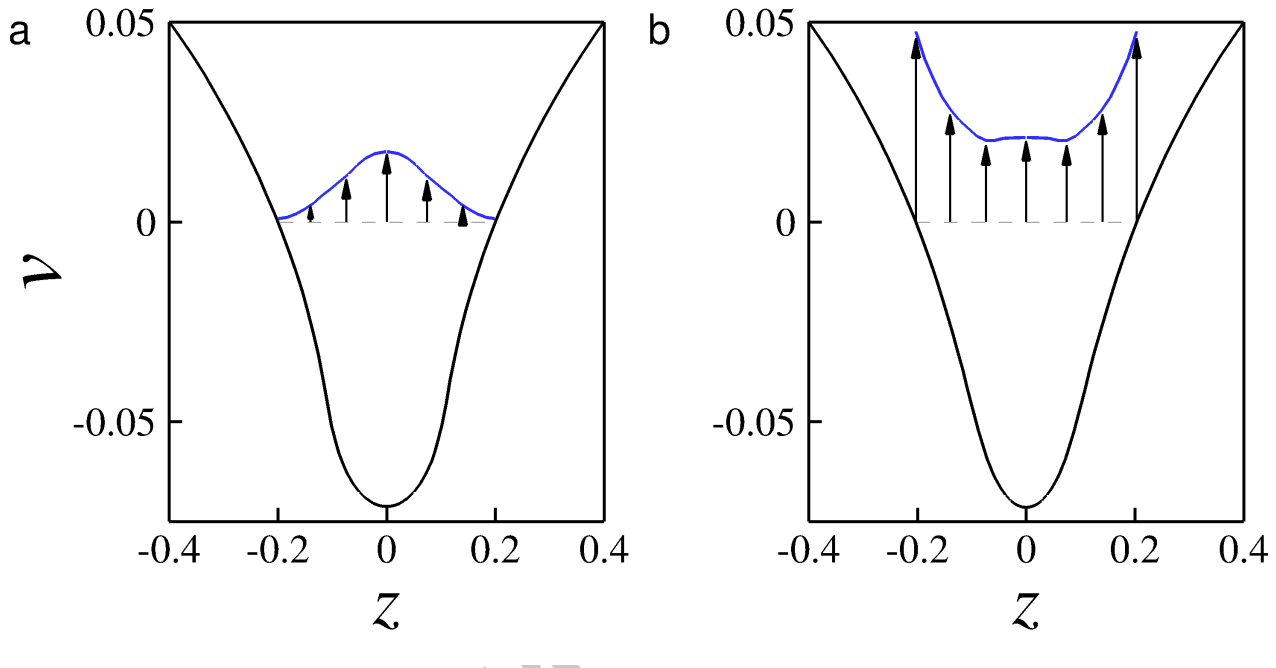

Figure 8: **Cross sectional velocity profile.** Radial velocity profiles (blue) corresponding to the instances shown in Figure 7 (a) and (c). Computations were carried out with elasticity numbers $\beta = 0$ and 5. Here, the black solid lines marks the interfacial profiles of the coalescing bubbles.

We model the coalescence of small bubbles with surfactants.

$\Rightarrow$

Surfactant accumulates on the meniscus bridge between the bubbles at the early time.

$\Rightarrow$

The surfactant is transported to the back of the bubbles by Marangoni stresses.

$\Rightarrow$

These coupled mechanisms retards the bubble coalescence rate.